Supplementary Information for

Generation and manipulation of chiral terahertz waves emitted from the three-dimensional topological insulator Bi_2Te_3

Haihui Zhao[a†], Xinhou Chen[b†], Chen Ouyang[c,e†], Hangtian Wang[a,d†], Deyin Kong[b], Peidi Yang[b], Baolong Zhang[c,e], Chun Wang[c,e], Gaoshuai Wei[c,e], Tianxiao Nie[a,d*], Weisheng Zhao[a,d*], Jungang Miao[b], Yutong Li[c,e], Li Wang[c*], and Xiaojun Wu[b,f*]

[a]Beihang University, Fert Beijing Institute, BDBC, and School of Microelectronics, Beijing, China, 100191
[b]Beihang University, School of Electronic and Information Engineering, Beijing, China, 100083
[c]Beijing National Laboratory for Condensed Matter Physics, Institute of Physics, Chinese Academy of Sciences, Beijing, China, 100190
[d]Beihang University, Beihang-Goertek Joint Microelectronics Institute, Qingdao Research Institute, Qingdao, China, 266000
[e]University of Chinese Academy of Sciences, School of Physical Sciences, Beijing, China, 100049
[f]Huazhong University of Science and Technology, Wuhan National Laboratory for Optoelectronics, Wuhan, China, 430074

correspondence to: xiaojunwu@buaa.edu.cn; nietianxiao@buaa.edu.cn;

weisheng.zhao@buaa.edu.cn; wangli@aphy.iphy.ac.cn

Supplementary Note 1

Sample characterization. The lattice structure of the molecular beam epitaxy (MBE) grown topological insulator samples with different thicknesses of 10 nm, 8 nm, and 5 nm examined in our experiments is exhibited in Fig. S1a and b. The surface lacks central inversion symmetry with the point group C_{3v} and the bulk space group is D_{3d}^5. Various characterization techniques including X-ray diffraction (XRD) and atomic force microscopy (AFM) have been carried out on the samples, and their corresponding results are illustrated in Fig. S1c-e. In addition, an atomic force microscopy image of the 10 nm Bi_2Te_3 is shown in Fig. S1c, which is the

indication of perfect morphology. A typical terrace character can be observed in the atomic force microscopy pattern. Fig. S1d shows the height of each step is ~1 nm, consistent with the thickness of one single QL layer (~0.955 nm). Thanks to the Van der Waals epitaxy mode, the relaxation generated from lattice mismatch was minimized during the growth, and the Bi_2Te_3 can grow on the sapphire with its own lattice constant, which can be verified by X-ray diffraction pattern shown in Fig. S1e. The results show sharp peaks belonging to 003 family, which is consistent with the hexagonal crystal structure of topological insulators, indicating the high quality of our films.

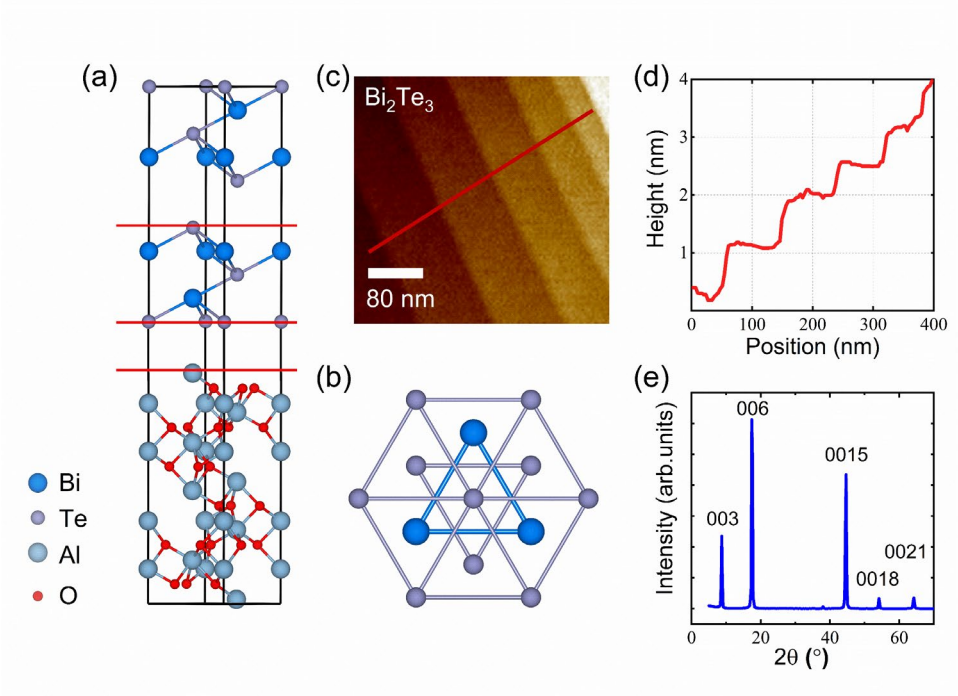

Fig. S1. Sample characterization. (a), Lattice structure of Bi_2Te_3 and Al_2O_3. Along the y-direction, the lattice consists of alternating layer of Bi and Te atoms. Five consecutive layers, termed quintuple layer (QL), make up the building block of the lattice. The top right corner is the top view of the material. (b), Top view of Bi_2Te_3. c, atomic force microscopy image of the sample, showing an atomically flat terrace with 1 QL steps. d, The height of the terrace along the red line in the image, showing a step size of ~1 nm. (e), X-ray diffraction spectrum of the sample in $\omega - 2\theta$ between 2θ =0° to 70°.

Supplementary Note 2

Comparison of terahertz emission from topological insulator and ZnTe. Under the same pump fluence of 16 μJ/cm^2, the emitted terahertz electric fields from 10 nm thick Bi_2Te_3 and 1 mm ZnTe nonlinear crystal are compared in Fig. S2a. The single-cycle terahertz signal from 10 nm thick Bi_2Te_3 is ~1/20 of that from 1 mm thick ZnTe crystal. The normalized emitted terahertz wave amplitude of Bi_2Te_3 is 2500 times larger than that of ZnTe, as shown in Fig. S2c. With higher freedom of functionality and comparable signal to noise ratio, topological insulators have the capability to be applied for real applications such as terahertz circular dichroism spectroscopy, other polarization-based imaging and secure communications. The frequency ranges from topological insulator and ZnTe can both cover up to 2.5 THz. This shows that the topological insulators can be comparable to the conversional ZnTe nonlinear crystal, and its high efficiency enables obvious advantages and application prospects on integrated terahertz devices and polarization sensitive investigations.

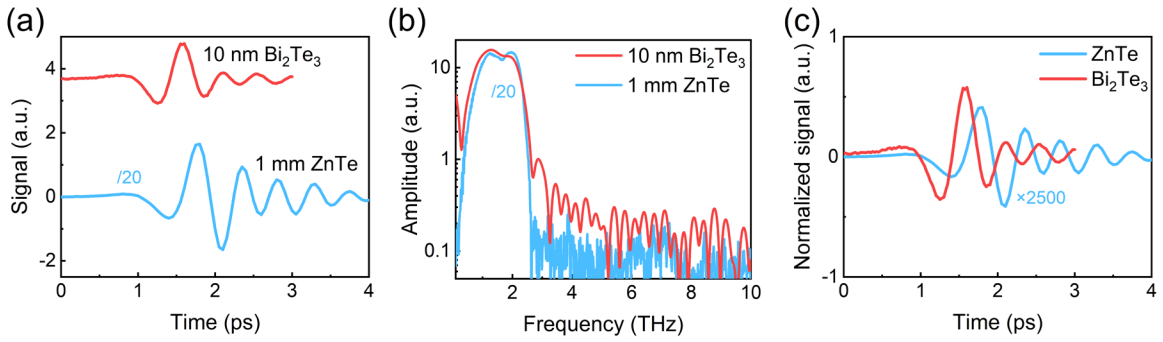

Fig. S2. Terahertz emission signal comparison between 10 nm Bi_2Te_3 nanofilm and 1 mm thick ZnTe crystal. (a), Terahertz temporal waveforms from the Bi_2Te_3 and ZnTe under the excitation of 16 μJ/cm^2, and (b), their corresponding spectra. (c), The comparation of normalized emitted terahertz wave amplitude between Bi_2Te_3 and ZnTe.

Supplementary Note 3

Terahertz temporal waveform and its corresponding spectrum as a function of the sample azimuthal angle. Fig. S3 illustrate the emitted terahertz temporal components of $S_x(t)$ and $S_y(t)$ for various sample azimuthal angles under p-polarized pump laser pulses. When the relative azimuthal angle is 0°, $S_x(t)$ signal is hard to be resolved. However, the signal continuously increases when the azimuthal angles varies from 0° to 30°. Such behavior starts to reversal from 30° to 60°. When the azimuthal angle changes from 60° to 120°, the terahertz polarity reversal but the variation regularity follows that from 0° to 60°. For $S_y(t)$ component, their terahertz phases for a specific azimuthal angle are opposite. The terahertz intensities decrease from 0° to 30°, but increases from 30° to 60°. From 60° to 120°, the terahertz signals also follow the rule as those in 0° to 60°, but the temporal waveforms have the opposite sign. These experimental results indicate the three-fold period when rotating the sample azimuthal angle, which phenomenologically corresponds to the linear photogalvanic effect as the predominant terahertz radiation mechanism.

The corresponding terahertz spectra are plotted in Fig. S3c and d. For all the examined azimuthal angles, the radiated terahertz spectra cover from 0.1 THz to 2 THz, and there are no distinct absorption features in the frequency range.

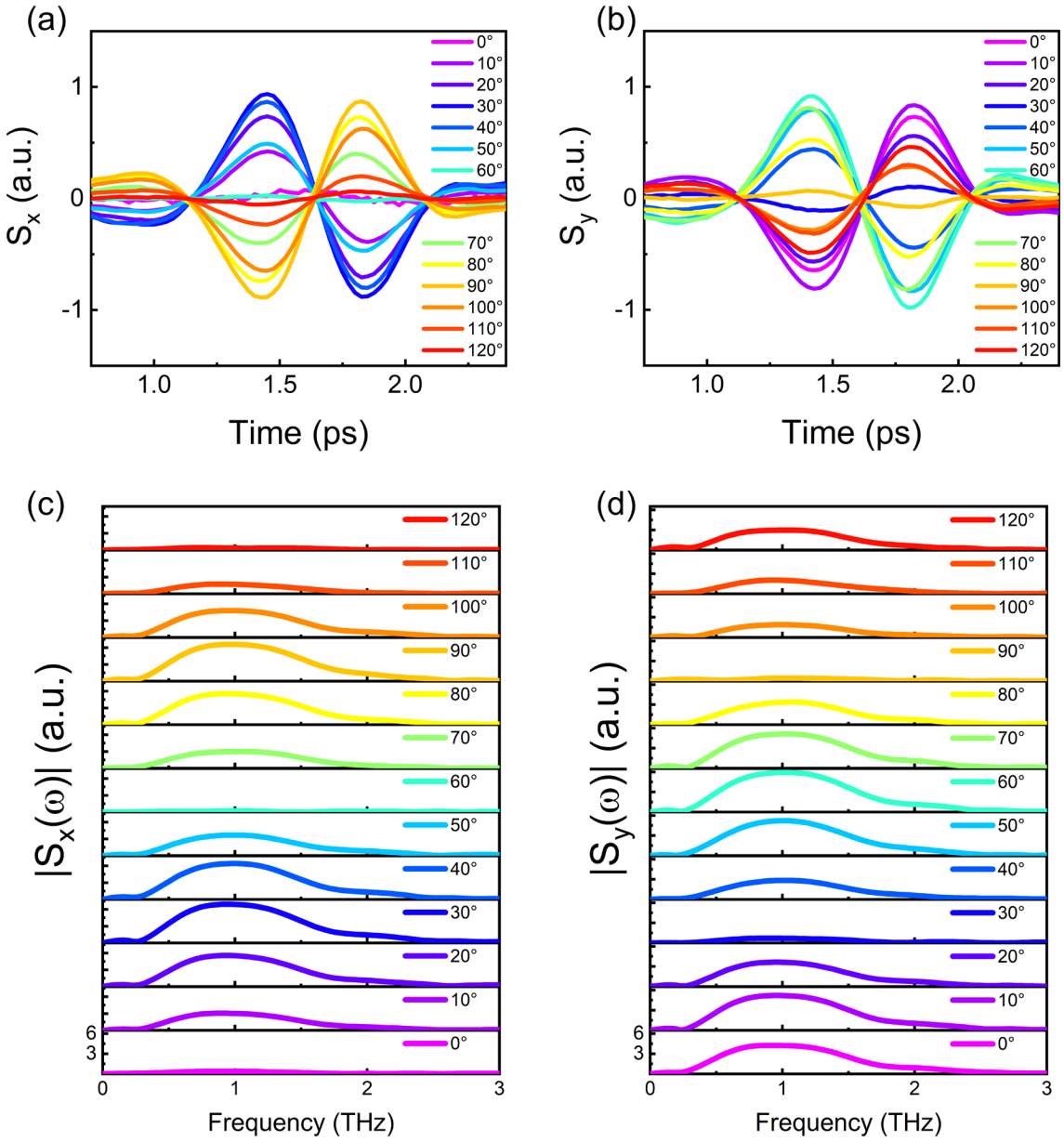

Fig. S3. Radiated terahertz temporal waveforms and their corresponding spectra in 10 nm Bi_2Te_3 for different sample azimuthal angles. (a), Emitted terahertz temporal components of $S_x(t)$ for the sample azimuthal angles from 0° to 120° with 10° interval, when pumped by p-polarized femtosecond laser pulses, and (b), for $S_y(t)$ component, respectively. (c) and (d), The corresponding spectra for several typical signals.

Supplementary Note 4

The mechanism of linearly polarized terahertz emission. In order to rule out the LPDE, we varied the incidence angle with different signs in Fig. S4a and b. If the LPDE played an important role within the interaction process, we would observe polarity reversal for terahertz waves. Nonetheless, we didn't observe such reversed signals along both x- and y-axis that LPDE was safely removed.

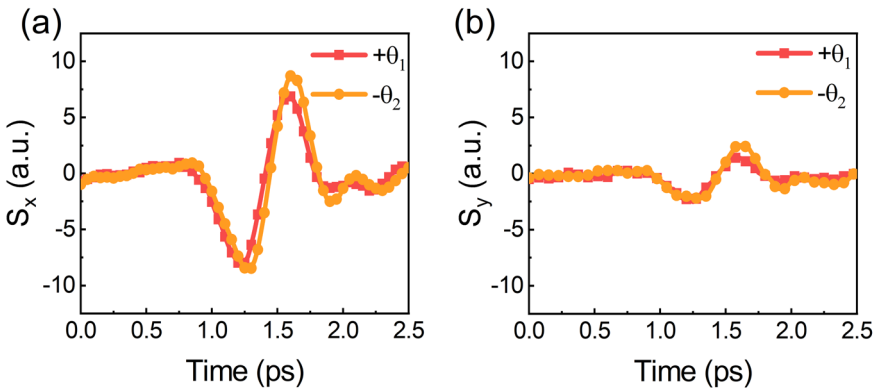

Fig. S4. Incidence angle dependent terahertz emission. Emitted terahertz temporal components of (a) $S_x(t)$ and (b) $S_y(t)$ from 10 nm thick Bi_2Te_3, respectively, excited by p-polarized laser pulses with positive and negative incidence angles of θ. The radiated terahertz polarity for both components show no reversal behavior manifesting the photon drag effect is not the predominant radiation mechanism.

The coefficients extracted by Eq. (1) in the main text along the x-axis (Fig. S5) have a very large B component, implying that the terahertz signals have a three-fold symmetry which is consistent with surface point group C_{3v} of Bi_2Te_3. It strongly demonstrates that the LPGE, namely, shift current dominates the linearly polarized terahertz emission. For the sake of semiquantitative comparison between the theoretical shift current and experimental data, we retrieved the normalized near-field photocurrent through following two steps.

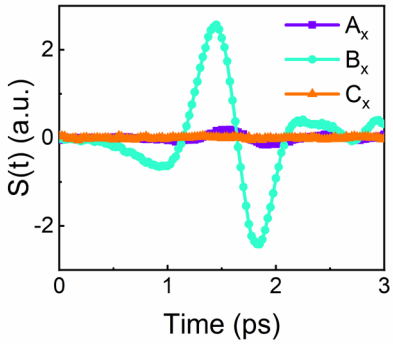

Fig. S5. Verification of linear photogalvanic effects as terahertz radiation mechanism. Parameters in x-direction extracted through the symmetry analysis of surface state using Eq. (1) in the main text.

For the first step, having the knowledge of transfer functions of propagating through the air (Fig. S6a) and relatively flat transfer function of ZnTe crystal, we can obtain the electric field of terahertz amplitude in frequency domain (Fig. S6c) via electro-optical signal (Fig. S6b).

For the second step, we extracted the data of real part of refractive index (Fig. S6d) in Ref. [36], and get the use of the generalized Ohm's law mentioned in methods to retrieve the amplitude of photocurrent in frequency domain. Finally, through inverse Fourier transformation, we got the near-field photocurrent near the surface of Bi_2Te_3.

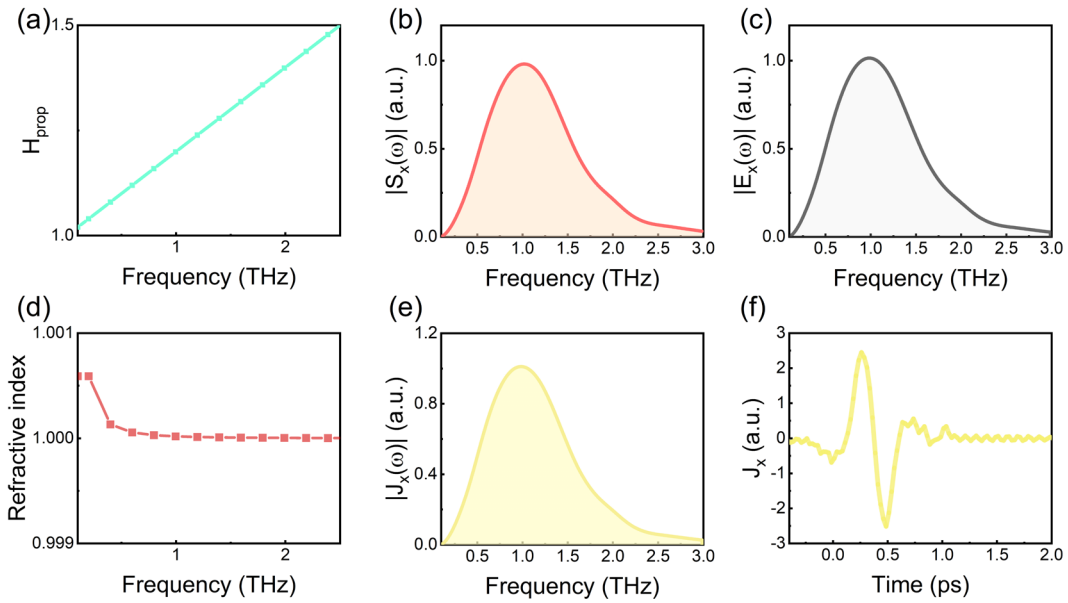

Fig. S6. Retrieving process of shift currents from probed far-field terahertz signals. (a), Transfer function H_{prop} describing the propagation from the sample to the electrooptic detection crystal between 0-2.5 THz. (b), Fourier transformed spectra of terahertz signals $S_x(t)$. (c), Calculated spectra of terahertz electric fields from the transfer function and the signal spectra. (d), Real part of refractive index of Bi_2Te_3 at the terahertz frequency range. (e), Retrieved spectra of the shift current according to the equation (9) in the main text. (f), Time domain trace of shift current J_x .

Supplementary Note 5

Ellipticity spectrum, phase difference of a high quality circularly polarized terahertz beam generation. Fig. S7a exhibits the high quality circularly polarized terahertz beams radiated from 10 nm thick Bi_2Te_3 obtained from an elliptically polarized pump beam with 16.0 μJ/cm^{37} pump fluence. The terahertz beam is left-handed polarized, and its ellipticity spectrum is shown in Fig. S7b. From this figure, we can see that the ellipticity reaches up to a maximum value of 0.95 at 0.5 THz. For the whole frequency range from 0.2 THz to 3.0 THz, the ellipticity keeps >0.4, which makes the possible the time-domain signal drawn in the Lissajous curve very close to the perfect circle. We can also observe that within 3 THz, the phase difference between the two components of the terahertz is around 100° to 120° from Fig. S7c. This indicates that the topological insulators we used are chiral broadband terahertz sources. According to the phase difference shown in Fig. S7c, the polarization states of the emitted

terahertz signals at 0.5 THz, 1.0 THz and 2.0 THz can be drawn out, as shown in the insets of Fig. S7d.

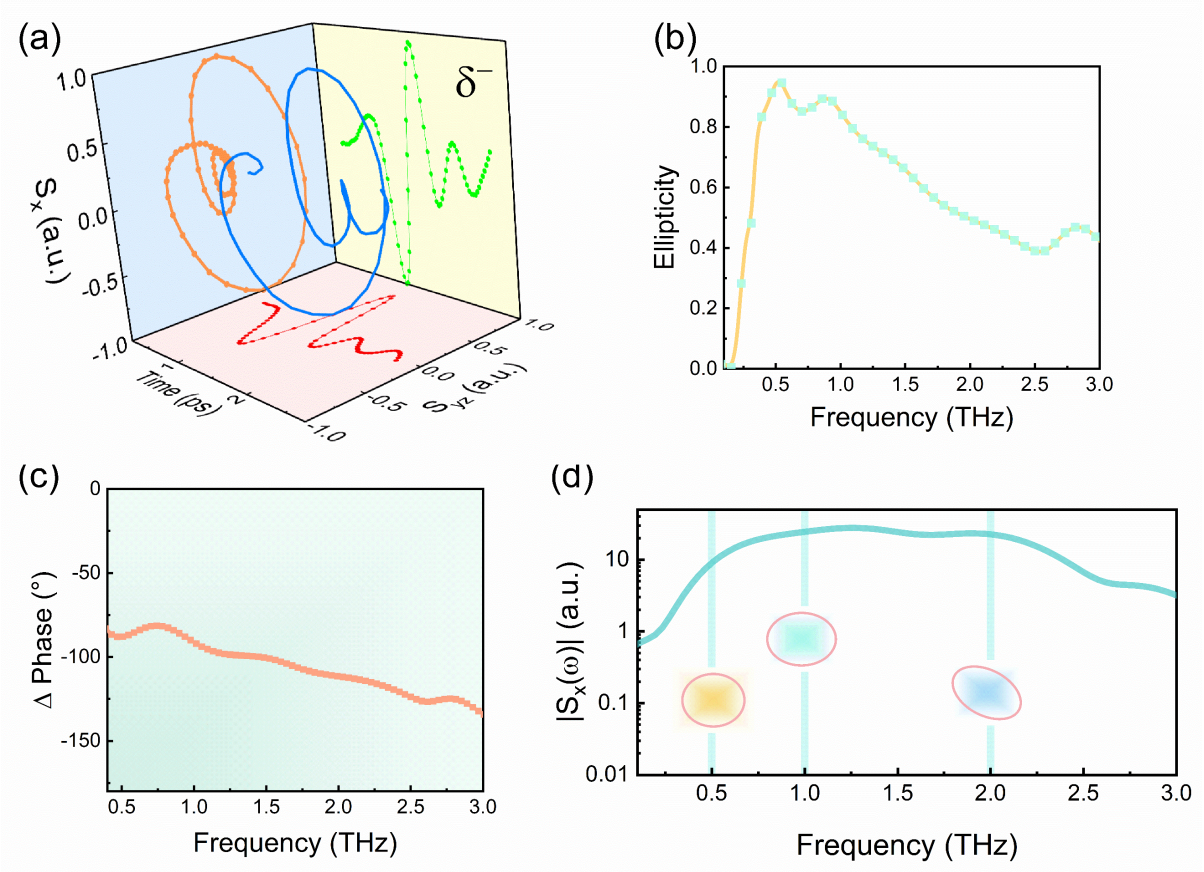

Fig. S7. High quality circularly polarized terahertz beam. (a), Circularly polarized terahertz polarization trajectories ($S_x(t)$, $S_{yz}(t)$) from 10 nm thick Bi_2Te_3. (b), Ellipticity spectrum of the circular terahertz wave. (c), Phase difference between $S_x(t)$ and $S_{yz}(t)$, $\Delta phase = \varphi_x - \varphi_{yz}$,where φ_x and φ_{yz} are the phases of $S_x(t)$ and $S_{yz}(t)$, respectively. (d), The Fourier transformed spectra of $S_x(t)$.

Supplementary Note 6

Macroscopic phenomenological PGE theory derivation. According to the pump-fluence-dependent experiment, we can clearly know that the second-order nonlinear optical response that occurs in the topological insulator. PGE is a known second-order nonlinear optical

response process, so we attempt to illustrate the underlying mechanism under a phenomenological PGE framework, which is generally expressed as[2]:

$$j_\lambda = \sigma_{\lambda\mu\nu} E_\mu(\omega) E_\nu^*(\omega), (\lambda, \mu, \nu = x, y, z) \quad \text{(S1)}$$

Here we imply Einstein's summation convention, $\sigma_{\lambda\mu\nu}$ is the third-order photoconductor tensor and $E_\beta(\omega) = E_\beta^*(-\omega)$ is the amplitude of the complex photoelectric field. The real oscillating photoelectric field can be written in this form $\varepsilon(t) = E(\omega)e^{i\omega t} + E^*(\omega)e^{-i\omega t}$. Under space inversion symmetric operation, $E_\mu(\omega) \to -E_\mu(\omega)$, $E_\nu^*(\omega) \to -E_\nu^*(\omega)$. Therefore, the product of the complex electric field remains unchanged, but the photocurrent will be inverted under the inversion operation, $j_\lambda \to -j_\lambda$. Any tensor describing the physical properties of a system is invariant under the symmetry operation of the system. Therefore, as to a system with spatial inversion symmetry, $\sigma_{\lambda\mu\nu}$ is invariant under spatial inversion. For tensor of odd order, inversion symmetry leads to $\sigma_{\lambda\mu\nu} \to -\sigma_{\lambda\mu\nu}$. Thus, $\sigma_{\lambda\mu\nu}$ vanishes in the system of inversion symmetry, which is exactly the case in the bulk region of Bi_2Te_3, and only leads to the nonlinear response on the surface region. We should only take the surface symmetry into account in our case.

The photocurrent must be a real number, so $j_\lambda^* = j_\lambda$. According to the Eq. (1), $j_\lambda^* = \sigma_{\lambda\mu\nu}^* E_\mu^*(\omega) E_\nu(\omega)$. Because μ, ν are dummy indexes, exchanging the position between them doesn't affect the result, so $j_\lambda^* = \sigma_{\lambda\nu\mu}^* E_\nu^*(\omega) E_\mu(\omega)$, resulting in $\sigma_{\lambda\mu\nu} = \sigma_{\lambda\nu\mu}^*$. This tells us that the real part of $\sigma_{\lambda\mu\nu}$ is symmetric for the last two indexes, i.e., $\mathrm{Re}(\sigma_{\lambda\mu\nu}) = \mathrm{Re}(\sigma_{\lambda\nu\mu})$, and the image part of $\sigma_{\lambda\mu\nu}$ is antisymmetric, i.e., $\mathrm{Im}(\sigma_{\lambda\mu\nu}) = -\mathrm{Im}(\sigma_{\lambda\nu\mu})$. By employing this property, we can write the photocurrent in a form $j_\lambda = \left[\mathrm{Re}(\sigma_{\lambda\mu\nu}) + i\,\mathrm{Im}(\sigma_{\lambda\mu\nu})\right] E_\mu E_\nu^* = \mathrm{Re}(\sigma_{\lambda\mu\nu}) E_\mu E_\nu^* + i\,\mathrm{Im}(\sigma_{\lambda\mu\nu}) E_\mu E_\nu^*$, the first term can be written to be:

$$\mathrm{Re}\left(\sigma_{\lambda\mu\nu}\right)E_\mu E_\nu^{*}=\frac{1}{2}\left[\mathrm{Re}\left(\sigma_{\lambda\mu\nu}\right)E_\mu E_\nu^{*}+\mathrm{Re}\left(\sigma_{\lambda\nu\mu}\right)E_\nu E_\mu^{*}\right]=\frac{1}{2}\mathrm{Re}\left(\sigma_{\lambda\mu\nu}\right)\left(E_\mu E_\nu^{*}+E_\nu E_\mu^{*}\right) \tag{S2}$$

while the second term can be written as:

$$i\,\mathrm{Im}\left(\sigma_{\lambda\mu\nu}\right)E_\mu E_\nu^{*}=\frac{i}{2}\left[\mathrm{Im}\left(\sigma_{\lambda\mu\nu}\right)E_\mu E_\nu^{*}+\mathrm{Im}\left(\sigma_{\lambda\nu\mu}\right)E_\nu E_\mu^{*}\right]=\frac{i}{2}\mathrm{Im}\left(\sigma_{\lambda\mu\nu}\right)\left(E_\mu E_\nu^{*}-E_\nu E_\mu^{*}\right) \tag{S3}$$

Accordingly, Eq. (S1) can be transferred to be:

$$j_\lambda=\frac{i}{2}\mathrm{Im}\left(\sigma_{\lambda\mu\nu}\right)\left(E_\mu E_\nu^{*}-E_\nu E_\mu^{*}\right)+\frac{1}{2}\mathrm{Re}\left(\sigma_{\lambda\mu\nu}\right)\left(E_\mu E_\nu^{*}+E_\nu E_\mu^{*}\right) \tag{S4}$$

The first term can be written as a cross product form, so we can obtain the following equation:

$$j_\lambda=i\gamma_{\lambda\mu}\left(\hat{E}\times\hat{E}^{*}\right)_\mu+\chi_{\lambda\mu\nu}\left(E_\mu E_\nu^{*}+E_\mu^{*}E_\nu\right) \tag{S5}$$

γ is related to the image part of $\sigma_{\lambda\mu\nu}$, $\chi_{\lambda\mu\nu}=\frac{1}{2}\mathrm{Re}\left(\sigma_{\lambda\mu\nu}\right)$, the last two indexes are symmetric such that $\chi_{\lambda\mu\nu}=\chi_{\lambda\nu\mu}$.

We now apply the Eq. (S5) in a more specific context, namely, the surface of topological insulator Bi_2Te_3. The first term of Eq. (S5) depicts the spin-polarized light, representing the CPGE, and vanishes for the linear polarized light. The surface of Bi_2Te_3 owns C_{3v} symmetry, corresponding to the three-fold rotation symmetry around the *z*-axis and three mirror reflection symmetry in the x-y plane. In the situation of rotating 2π/3 around the *z*-axis, $\left(\hat{E}\times\hat{E}^{*}\right)_\mu\rightarrow\mathbf{R}\left(\hat{E}\times\hat{E}^{*}\right)_\mu$, $j\rightarrow\mathbf{R}j$, $\mathbf{R}=\begin{pmatrix}\cos\left(\frac{2\pi}{3}\right) & -\sin\left(\frac{2\pi}{3}\right) & 0\\ \sin\left(\frac{2\pi}{3}\right) & \cos\left(\frac{2\pi}{3}\right) & 0\\ 0 & 0 & 1\end{pmatrix}$. Thus, we get the relation $\mathbf{R}\hat{j}=i\gamma\mathbf{R}\left(\hat{E}\times\hat{E}^{*}\right)$, substitute the photocurrent j on the left side of this equation with $i\gamma\left(\hat{E}\times\hat{E}^{*}\right)$, you can get $\mathbf{R}\gamma=\gamma\mathbf{R}$. To satisfy this constrained condition, γ must possess the form of $\begin{pmatrix}\gamma_{xx} & \gamma_{xy} & 0\\ -\gamma_{xy} & \gamma_{yy} & 0\\ 0 & 0 & \gamma_{zz}\end{pmatrix}$, and then the mirror reflection will constrain γ further. Suppose that the

intersection angle between one mirror and x-axis is φ, the operation of mirror reflection can be written as $\mathbf{M}=\begin{pmatrix}\cos(2\varphi) & \sin(2\varphi) & 0\\ -\sin(2\varphi) & \cos(2\varphi) & 0\\ 0 & 0 & 1\end{pmatrix}$. The photocurrent under the operation of reflection can be $j \to \mathbf{M}j$. However, as a pseudo-vector, $\left(\hat{E}\times\hat{E}^*\right)_\mu \to -\mathbf{M}\left(\hat{E}\times\hat{E}^*\right)_\mu$, thus, we get the relation $\mathbf{M}\gamma=-\gamma\mathbf{M}$. Eventually, under the consideration of $\mathbf{R}$ and $\mathbf{M}$, γ must have the form as $\begin{pmatrix}0 & \gamma_{xy} & 0\\ -\gamma_{xy} & 0 & 0\\ 0 & 0 & 0\end{pmatrix}$. Let $\gamma_{xy}=-\gamma_{yx}=\gamma$, we can get a compact form of CPGE induced photocurrent as follows:

$$j_{CPGE}=i\gamma\left[\left(E_zE_x^*-E_xE_z^*\right)\hat{x}-\left(E_yE_z^*-E_zE_y^*\right)\hat{y}\right] \tag{S6}$$

From Eq. (S6), we can easily get the conclusion that CPGE won't induce any photocurrent under normal incidence, i.e., when $E_z=0$.

From now on, let's look at the second term of Eq. (S5). On the one hand, under the rotation operation, the final photocurrent will be $\hat{j}'=\mathbf{R}\hat{j}=i2\begin{pmatrix}R_{xx}\chi_{xij}+R_{xy}\chi_{yij}\\ R_{yx}\chi_{xij}+R_{yy}\chi_{yij}\\ \chi_{zij}\end{pmatrix}E_iE_j^*$. On the other hand, $\hat{j}'=i2\begin{pmatrix}\chi_{xij}R_{ik}E_kR_{js}E_s^*\\ \chi_{yij}R_{ik}E_kR_{js}E_s^*\\ \chi_{zij}R_{ik}E_kR_{js}E_s^*\end{pmatrix}$, with the symmetric condition that $\chi_{\lambda\mu\nu}=\chi_{\lambda\nu\mu}$, we can reduce the number of the components of χ to 18. Besides, adding the mirror reflection operation, we obtain that $\begin{pmatrix}M_{xx}\chi_{xij}+M_{xy}\chi_{yij}\\ M_{yx}\chi_{xij}+M_{yy}\chi_{yij}\\ \chi_{zij}\end{pmatrix}E_iE_j^*=\begin{pmatrix}\chi_{xij}M_{ik}E_kM_{js}E_s^*\\ \chi_{yij}M_{ik}E_kM_{js}E_s^*\\ \chi_{zij}M_{ik}E_kM_{js}E_s^*\end{pmatrix}$. After considering these conditions, we finally calculate four independent tensor elements for χ. Those are $\chi_{yyy}=-\chi_{yxx}=-\chi_{xxy}=-\chi_{yyx}$, $\chi_{zyy}=\chi_{zxx}$, $\chi_{yyz}=\chi_{yzy}=\chi_{xxz}=\chi_{xzx}$, χ_{zzz}, all other elements vanish. As a result, the components of LPGE photocurrent are as follow:

$$j_x = -2\chi_{yyy}\left(E_x E_y^* + E_y E_x^*\right) + 2\chi_{yyz}\left(E_x E_z^* + E_z E_x^*\right) \tag{S7}$$

$$j_y = 2\chi_{yyy}\left(\left|E_y\right|^2 - \left|E_x\right|^2\right) + 2\chi_{yyz}\left(E_y E_z^* + E_z E_y^*\right) \tag{S8}$$

$$j_z = 2\chi_{zzz}\left|E_z\right|^2 + 2\chi_{zyy}\left(\left|E_y\right|^2 + \left|E_x\right|^2\right) \tag{S9}$$

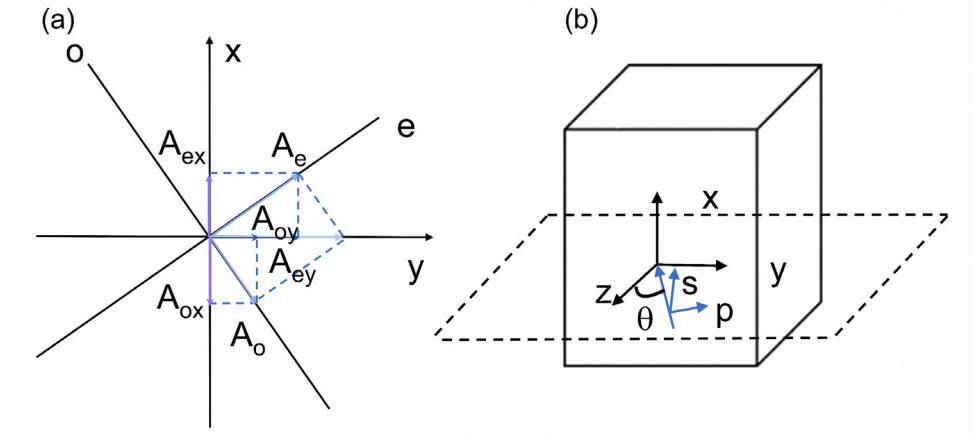

Fig. S8. Geometric layout of incidence laser polarization state and sample surfaces. (a), Components when the quarter wave plate angle is α. (b), The geometric layout.

Supposed that the intersection angle between the incident plane and x-axis is φ, the incident angle is θ, the rotated angle of quarter wave plate is α, and then we can obtain the complex electric component of arbitrary direction as following[38]:

$$E(\omega) = -\frac{i\omega A_0}{2}\begin{pmatrix} -\sin 2\alpha \sin\varphi - (i+\cos 2\alpha)\cos\theta\cos\varphi \\ \sin 2\alpha\cos\varphi - (i+\cos 2\alpha)\cos\theta\sin\varphi \\ (i+\cos 2\alpha)\sin\theta \end{pmatrix} \tag{S10}$$

$$E^*(\omega) = \frac{i\omega A_0}{2}\begin{pmatrix} -\sin 2\alpha \sin\varphi - (-i+\cos 2\alpha)\cos\theta\cos\varphi \\ \sin 2\alpha\cos\varphi - (-i+\cos 2\alpha)\cos\theta\sin\varphi \\ (-i+\cos 2\alpha)\sin\theta \end{pmatrix} \tag{S11}$$

In our case, the incident laser pulse was shining on the y-z plane, namely, $\varphi = \pi/2$, thus, $\sin\varphi = 1$, and $\cos\varphi = 0$. We will get the following equations:

$$E(\omega) = -\frac{i\omega A_0}{2}\begin{pmatrix} -\sin 2\alpha \\ -(i+\cos 2\alpha)\cos\theta \\ (i+\cos 2\alpha)\sin\theta \end{pmatrix} \tag{S12}$$

$$E^*(\omega)=\frac{i\omega A_0}{2}\begin{pmatrix}-\sin 2\alpha\\ (i-\cos 2\alpha)\cos\theta\\ (-i+\cos 2\alpha)\sin\theta\end{pmatrix} \tag{S13}$$

By inserting these two components to Eq. (S6), we will get the CPGE induced photocurrent:

$$j_{CPGE}=-2\gamma C^2\begin{pmatrix}\sin 2\alpha\sin\theta\\ 0\\ 0\end{pmatrix},\ C=\frac{\omega A_0}{2} \tag{S14}$$

As for the LPGE induced photocurrent, let $\chi_{yyy}=\eta_1$, $\chi_{yyz}=\eta_2$, $\chi_{zzz}=\eta_3$, $\chi_{zyy}=\eta_4$ for brevity, we can write the final LPGE in a compact way, $j_{LPGE}=\begin{pmatrix}j_x\\ j_y\\ j_z\end{pmatrix}$, all components are read as:

$$j_x=-2C^2(\eta_1\cos\theta+\eta_2\sin\theta)\sin 4\alpha \tag{S15}$$

$$j_y=2C^2\left(\eta_1\left(\frac{1}{2}\cos^2\theta+\frac{1}{2}\right)-\eta_2\sin\theta\cos\theta\right)\cos 4\alpha+2C^2\left(\eta_1\left(\frac{3}{2}\cos^2\theta-\frac{1}{2}\right)-3\eta_2\sin\theta\cos\theta\right) \tag{S16}$$

$$j_z=2C^2\left(\eta_3\frac{1}{2}\sin^2\theta+\eta_4\left(\frac{1}{2}\cos^2\theta-\frac{1}{2}\right)\right)\cos 4\alpha+2C^2\left(\eta_3\frac{3}{2}\sin^2\theta+\eta_4\left(\frac{1}{2}+\frac{3}{2}\cos^2\theta\right)\right) \tag{S17}$$

These four equations are all about the CPGE and LPGE induced components of photocurrent. For incident laser with arbitrary polarization and directions, the LPGE induced photocurrent can be written in a form of $j_{LPGE}=j_{LPGE,1}\sin 4\alpha+j_{LPGE,2}\cos 4\alpha+j_{LPGE,3}$, that's why we can write the emitted THz signals in a form of Eq. (S3) in the main text.